sciendo

DOI 10.2478/ama-2023-0015

acta mechanica et automatica, vol.17 no.1 (2023
Special Issue "Computational Technologies in Engineering TKI2022"

FAILURE ANALYSIS OF BEAM COMPOSITE ELEMENTS SUBJECTED TO THREE-POINT BENDING USING ADVANCED NUMERICAL DAMAGE MODELS

Patryk RÓŻYŁO*

*Faculty of Mechanical Engineering, Department of Machine Design and Mechatronics, Lublin University of Technology, ul. Nadbystrzycka 36, 20-618 Lublin, Poland

p.rozylo@pollub.pl

received 11 November 2022, revised 4 December 2022, accepted 4 December 2022

Abstract: This paper deals with the experimental and numerical analysis of three-point bending phenomenon on beam composite profiles. Flat rectangular test specimens made of carbon–epoxy composite, characterised by symmetric [0/90/0/90]s laminate ply lay-up, were used in this study. Experimental testing was carried out with a COMETECH universal testing machine, using special three-point bending heads. In addition, macroscopic evaluation was performed experimentally using a KEYENCE Digital Microscope with a mobile head recording real-time images. Parallel to the experimental studies, numerical simulations were performed using the finite element method in ABAQUS software. The application of the above-mentioned interdisciplinary research techniques allowed for a thorough analysis of the phenomenon of failure of the composite material subjected to bending. The obtained research results provided a better understanding of the failure mechanism of the composite material.

Key words: three-point bending, carbon–epoxy laminate, numerical simulation, experimental tests, finite element method, failure

1. INTRODUCTION

Beam composite structures are commonly used for stiffening elements in the aerospace, construction and automotive industries. These types of structures are primarily subjected to compression and bending. In the case of compression of beam structures, many additional phenomena occur, such as loss of stability and complex failure mechanism, as described in detail by the authors of many research papers [1–3]. The prediction of the maximum load of composite structure is still very desirable. The composite materials are still expansive group of materials which are characterised by the occurrence of multiple complex forms of damage, thus requiring in-depth research. Besides a series of already known behaviours of beam composite structures that occur in axial [4], or eccentric compression [5–9], it is also important to know the behaviour of the structure, in bending [10–14]. The cognitive value of the behaviour of beam structures made of composite materials is still very important, and despite the many studies conducted in this area, the behaviour of the structure subjected to bending taking into account the complex failure mechanism is not yet clearly defined.

Beam composite structures, regardless of the loading conditions to which they are subjected, are currently an area of interest for many researchers [15–18]. In the case of the bending behaviour of a structure, it is necessary to be able to correctly analyse the damage forms occurring as a result of the loading process on the structure. It is essential, above all, to estimate the loads that cause the limit states of the bending structure, as well as to register the damage forms that appear during the failure tests. Consequently, it is important to understand how to identify the damage phases that occur during testing. The above demands a comprehensive analysis, both on the basis of experimental studies and numerical simulations, using the finite element method (FEM), which enables to characterise the complex phenomenon of composite material failure, including the phenomena directly accompanying the failure [19–27]. The main theory that allows assessment of the damage initiation phenomenon in the case of composite materials–laminates is the first ply failure (FPF) theory [28]. This theory assumes that composite failure occurs when the first layer of the composite is damaged. The damage initiation can be determined by many factors, such as damage to the fibres or matrix of the composite material. Besides damage initiation, there are other phenomena that contribute to the failure of the composite material, such as delamination. It is important to evaluate the phenomena contributing to the degradation of the composite material structure.

The evaluation of the failure phenomenon is slightly different for experimental studies and numerical simulations using FEM. In the case of experimental research, usually the testing instruments such as universal testing machine (UTM) [19], acoustic emission method equipment [29] and others are used to evaluate the failure phenomenon of beam composite materials. As part of the experimental study, it is possible to estimate both loads and register damage forms of beam structures made of laminates [19, 27]. On the other hand, numerical simulations allow for a thorough estimation of any phenomena which directly contribute to the loss of load-carrying capacity of composite structures. Within the framework of numerical simulations using FEM, it is possible, among other things, to accurately determine the damage initiation phenomenon of a composite material using special damage models.

The widely used method of damage initiation assessment is based on the Hashin's criterion [30]. Based on the Hashin criterion, it can be evaluated whether the damage occurred due to failure of the fibres or matrix of the composite material, through compression or tension. This criterion allows assessment of damage initiation; however, after further consideration of the energy criterion, it is also possible to assess the damage evolution. Generally, the damage model allowing for damage initiation based on the Hashin criterion and damage evolution based on the energy criterion is called progressive failure analysis (PFA) [31–33]. The fundamentals of the described issues are based on the continuum damage mechanics (CDM) [34, 35], where the beginnings of the damage mechanisms description were presented in the paper [36], and the first model taking into account especially the damage initiation phenomenon within the framework of numerical simulations in the ABAQUS program was presented in the paper [37]. Many contemporary researchers have dealt with the analysis of the failure phenomenon of beam composite materials based on PFA, beginning with the paper [38] to more recent papers [39, 40]. Moreover, other very advanced damage models are available, which allow the simulation of delamination – a method based on the cohesive zone model (CZM). The above model provides an assessment of composite material damage as a result of simulation of permanent rupture of the connection between the constituent layers of the composite (both in the damage initiation – usually based on the criterion of maximum nominal stress (MAXS) and damage evolution, based on the energy criterion) [41–43]. The above-mentioned damage model is based on the traction-separation law (which describes the relationship between traction-stress in the material interface and adequate displacement peak, between two parts of a material being separated) [44, 45], where a graphical representation of this law is shown in the paper [46]. The phenomenon of delamination-induced damage has been thoroughly demonstrated in many research papers [47–52]. Furthermore, a commonly used damage model is the eXtended finite element method (XFEM), which allows the simulation of material cracking (fracture) [53–56]. The above-mentioned model offers the ability to reproduce the entire crack geometry independently of the adopted mesh, so that no sophisticated mesh is needed to model the crack growth. The methods described above allow evaluation of the complex failure mechanism of the composite material.

The scope of the study was primarily to conduct experimental tests and numerical simulations (using FEM) [57] of three-point bending of a beam composite structure. The experimental tests were carried out using a UTM and a digital microscope with a mobile head that allows recording the damage state of the composite material. In the case of numerical simulations, nonlinear analysis was carried out, taking into account two advanced damage models: a CZM allowing simulation of the delamination phenomenon (CZM) and a model allowing simulation of material crack initiation and propagation (XFEM). The use of independent numerical damage models allows a comprehensive assessment of the damage phenomenon [58, 59], which was verified experimentally [19, 20, 60]. It is necessary to employ interdisciplinary and independent research methods allowing for description of composite failure [61–66]. The primary objective of this study was to develop complex numerical models that allow for a comprehensive evaluation of the failure phenomenon enabling a better understanding of the experimental results.

2. METHODOLOGY OF THE STUDY

The test specimens were made of carbon–epoxy composite using autoclave technique. Ultimately, six specimens were prepared for experimental testing. The geometry of the specimens was selected so as to perform three-point bending tests over the full load range. The above-mentioned method of manufacturing of beam multilayer composite materials enabled to obtain a material structure with high structural properties, as well as the proportion of fibres relative to the whole structure in the range of 55%–60%, which is described in more detail in the papers [67, 68]. The use of the mentioned technique allows the production of composite profiles with high quality of material structure [67]. The columns under consideration were made by autoclaving technique using a vacuum package made on a special mould reproducing the shape and dimensions of the manufactured beams. The prepared hermetic package ensuring the maintenance of a vacuum of value of about −0.1 MPa was subjected to the polymerisation process in a laboratory autoclave, ensuring the required pressure by creating an additional overpressure in the autoclave of 0.4 MPa. In the case of the carbon–epoxy composite, a material heating temperature of 135°C for about 2 h was used to ensure completion of the pre-preg polymerisation process (Fig. 1.). In order to eliminate unfavourable phenomena that can occur during the manufacturing process (excessive increase of thermal stresses in the material and limitation of proper relaxation of primary and thermal stresses), precise control of the heating and cooling rate of 0.033 K/s was applied.

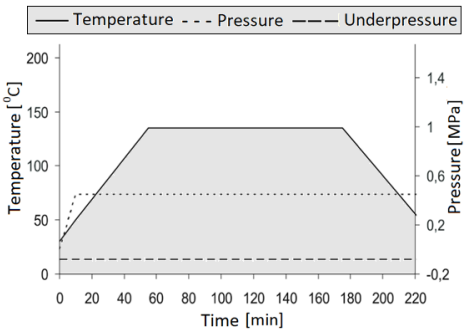

Fig. 1. Process of composite manufacturing

The manufactured composite specimens were characterised by a symmetrical stacking sequence of laminate layers [0/90/0/90]s which may be otherwise represented as [0/90/0/90/90/0/90/0]. The specimens consisted of eight layers, where the length and width of the specimens were 135 mm and 15 mm, respectively, and the thickness of each individual layer was 0.131 mm. A graphical representation of the test specimen is presented in Fig. 2.

The material properties of test specimens (six samples) were determined based on static tensile PN-EN ISO 527-5, compression PN-EN ISO 14126 as well as shear test PN-EN ISO 14129. The determined material properties were determined using the UTM – Tab. 1 [4, 19–21, 49, 64, 67, 69].

The experimental investigations were conducted primarily using a UTM COMETECH model QC-508 (type M2F). The machine was equipped with an NTS load cell with a maximum capacity of 2.5 kN. The machine had a special module for performing three-point bending tests. All the test parameters such as force and

displacement were registered using the Amis-Plus 1.5.6 software. The experimental tests were carried out at room temperature with a constant crosshead speed of 2 mm/min [70]. Moreover, a modern digital microscope from KEYENCE (model VHX 970F) was used in the experimental studies. The microscope had a special module containing a mobile (portable) measuring head, which was extremely useful in the framework of the conducted experimental tests of three-point bending. The mobile (portable) microscope head allowed for image capture with a maximum zoom of 200×, while in the present study a zoom of 30× was used, covering the most important area of damage to the laminate during the conducted tests. In addition, a special mechanical articulated arm having an attachment to a mobile (portable) digital microscope head was also used in the experimental study. The use of this arm made it possible to properly mount the microscope head in such a way as to be able to record the image associated with the area of damage to the composite structure. The test stand accessories are shown in Fig. 3.

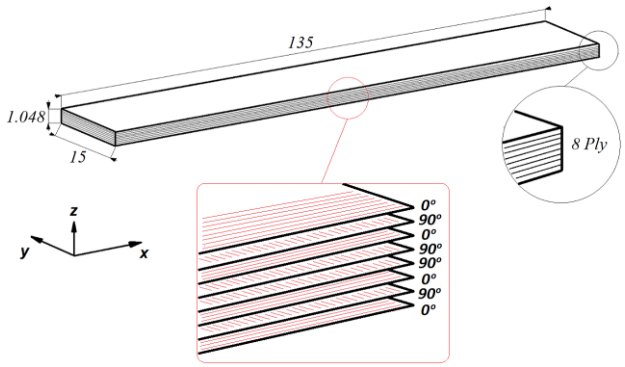

Fig. 2. Graphical representation of test specimens

Tab. 1. Mechanical properties of the composite material [19, 67, 68]

Mechanical Properties		Strength Properties	
Young' Modulus E_1 [MPa]	130710	Tensile Strength (0°) F_{T1} [MPa]	1867
Young' Modulus E_2 [MPa]	6360	Compressive Strength (0°) F_{C1} [MPa]	1531
Poisson's Ratio v_{12} [-]	0.32	Tensile Strength (90°) F_{T2} [MPa]	26
Kirchhoff modulus G_{12} [MPa]	4180	Compressive Strength (90°) F_{C2} [MPa]	214
		Shear Strength F_{12} [MPa]	100

a) b) c)

Fig. 3. Test stand: (a) UTM with three-point bending head, (b) digital microscope with mobile head and (c) articulated arm for microscope head

Experimental tests were carried out using the testing devices presented above, which made it possible to realise the process of three-point bending with simultaneous recording of test parameters, such as the force–displacement relationship, as well as recording of laminate failure forms. The tests were conducted in such a way that, in addition to recording the loading force and the displacement of the crosshead, the damage forms of the composite specimens were also registered, using a mobile microscope head mounted on an articulated arm, at a distance that allowed the correct recording of the images in digital form. The test stand during the experimental trials conducted is shown in Fig. 4.

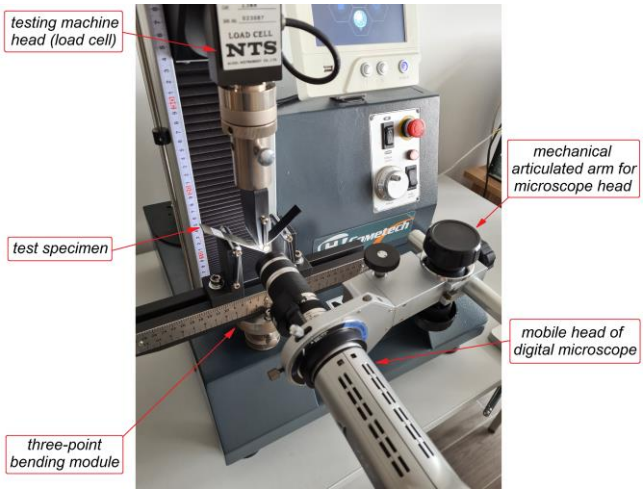

Fig. 4. Test stand during three-point bending test

During the experimental tests, loads corresponding to the loss of load-carrying capacity of the structure were registered, where complex phases of laminate failure such as fibre failure and delamination were observed, which was the direct cause of the decrease in load carried by the structure. The failure of the structure was observed both in the Amis-Plus 1.5.6 software, which was used to generate force–displacement characteristics, as well as within complex failure forms captured using a digital microscope head.

Numerical simulations using the FEM were conducted in ABAQUS. This advanced computational software made it possible to perform a comprehensive nonlinear analysis, including composite material failure (using static analysis). In the framework of numerical simulations, the author's numerical model was prepared in order to precisely represent the actual process of three-point bending realised on beam composite structures. The prepared finite element analysis (FEA) model had a material model with parameters compatible with the material properties shown in Tab. 1 (using Engineering Constants approach). The numerical model was developed to ensure full reproduction of the boundary conditions that actually occurred in the experimental studies. The numerical calculations were realised based on the Newton–Raphson incremental-iterative method, which is presented in detail in the paper [71]. The finite element (FE) models generated in ABAQUS program are usually nonlinear (and can involve from a few to thousands of variables). Regarding the above, the equilibrium equations obtained by discretising the virtual work equation can be represented using the equation:

$$F^N(u^M) = 0 \tag{1}$$

where F^N denotes the force component conjugate to the N^{th} variable in the problem and u^M constitutes the value of the M^{th} variable.

Numerical calculations generally use Newton's method (as a numerical method for solving the nonlinear equilibrium equations). The motivation for this choice is the convergence rate obtained by using the above-mentioned method compared with the modified Newton or quasi-Newton methods. Assume that, after an iteration i, an approximation uiM to the solution has been reached. Moreover, let ci+1M be the difference between this solution and the exact solution to the discrete equilibrium presented within the framework of Eq. (1). Regarding the above:

$$F^N(u_i^M + c_{i+1}^M) = 0 \tag{2}$$

By expanding the left-hand side of this equation (Taylor series) to an approximate solution, one obtains:

$$F^N(u_i^M) + \frac{\partial F^N}{\partial u^P}(u_i^M)c_{i+1}^P + \frac{\partial^2 F^N}{\partial u^P \partial u^Q}(u_i^M)c_{i+1}^P c_{i+1}^Q + .. = 0 \tag{3}$$

When u_i^M is a close approximation to the solution, the magnitude of any c_{i+1}^M will be small, so all of the above conditions except the first two can be neglected, giving a linear form of equations:

$$K_i^{NP} c_{i+1}^P = -F_i^N, \;\; K_i^{NP} = \frac{\partial F^N}{\partial u^P}(u_i^M), \;\; F_i^N = F^N(u_i^M) \tag{4}$$

A further approximation of the solution is:

$$u_{i+1}^M = u_i^M + c_{i+1}^M \tag{5}$$

and the iteration continues. The above relations describe the procedure of the method used to solve the nonlinear problem.

One of two damage models that was used to simulate the failure phenomenon was the CZM [19, 72]. The CZM allowed for the evaluation of the regions affected by delamination in the bending composite profiles. The above-mentioned damage model was based on a delamination technique using a cohesive surfaces approach. Numerical simulations were performed using the delamination technique based on the traction-separation law. The mechanical behaviour (in the elastic range) of the cohesive layer is characterised by nominal traction stress vector Eq. (6) [46, 73]:

$$t = \begin{Bmatrix} t_\mathrm{n} \\ t_\mathrm{s} \\ t_\mathrm{t} \end{Bmatrix} = \begin{bmatrix} K_\mathrm{nn} & K_\mathrm{ns} & K_\mathrm{nt} \\ K_\mathrm{ns} & K_\mathrm{ss} & K_\mathrm{st} \\ K_\mathrm{nt} & K_\mathrm{st} & K_\mathrm{tt} \end{bmatrix} \begin{Bmatrix} \delta_\mathrm{n} \\ \delta_\mathrm{s} \\ \delta_\mathrm{t} \end{Bmatrix} = K\delta. \tag{6}$$

where t, t_n, t_s and t_t are tractions in the cohesive layer; K, K_nn, K_ss and K_tt represent the cohesive layer stiffness and δ, δ_n, δ_s and δ_t are separation displacement of the cohesive layer (in global, normal, shear and transverse shear directions).

The damage initiation within the CZM for the numerical model adopted for the study was based on the MAXS criterion – MAXS. Damage initiation occurs when the relationship describing the damage initiation achieves a value of 1 [46, 73]:

$$\max\left\{\frac{\langle t_\mathrm{n}\rangle}{t_\mathrm{n}^0}, \frac{t_\mathrm{s}}{t_\mathrm{s}^0}, \frac{t_\mathrm{t}}{t_\mathrm{t}^0}\right\} = 1. \tag{7}$$

where t_n^0, t_s^0 and t_t^0 are peak values of the contact stress (when the separation is either purely normal, shear or transverse shear direction to the interface of material) and $\langle\ \rangle$ denotes Macaulay bracket (purely compressive stresses/strains do not cause damage initiation).

When the damage initiation is fulfilled, further loading of the composite structure causes damage evolution phenomenon. The damage evolution law describes the rate at which the cohesive stiffness is degraded once the corresponding damage initiation criterion is reached. In the case of damage evolution, the damage parameter D has been defined. A scalar damage parameter (monotonically evolves from 0 to 1), defines the overall damage directly at the contact point in the composite material. The contact stress components, in terms of the traction-separation law, are defined by appropriate conditions and expressed by the following relationships [46, 73]:

$$t_\mathrm{n} = \begin{cases} (1-D)\bar{t_\mathrm{n}}, & \bar{t_\mathrm{n}} \geq 0 \\ \bar{t_\mathrm{n}}, & \text{otherwise} \end{cases} \tag{8}$$

$$t_\mathrm{s} = (1-D)\bar{t_\mathrm{s}}, \tag{9}$$

$$t_\mathrm{t} = (1-D)\bar{t_\mathrm{t}}, \tag{10}$$

where t_n^-, t_s^- and t_t^- represent the stress components which were determined on the basis of the elastic traction-separation behaviour for the current separations (without material damage).

In order to describe the damage evolution under a combination of normal as well as shear separations (across the interface), it is useful to introduce an effective separation [72, 73]:

$$\delta_\mathrm{m} = \sqrt{\langle\delta_\mathrm{n}\rangle^2 + \delta_\mathrm{s}^2 + \delta_\mathrm{t}^2} \tag{11}$$

In the present study, the energy criterion was used to describe the damage evolution (using fracture energy parameters). Damage evolution phenomenon was defined using the Benzeggagh–Kenane (B–K) energy criterion [41]. Regarding the adopted damage evolution criterion, it is necessary to define the parameters: G_n^C, G_s^C as well as η. Regarding the above-mentioned criterion, $G_\mathrm{s}^\mathrm{C} = G_\mathrm{t}^\mathrm{C}$. The above-mentioned criterion is represented by the following relationships [46, 73]:

$$G^\mathrm{C} = G_\mathrm{n}^\mathrm{C} + (G_\mathrm{s}^\mathrm{C} - G_\mathrm{n}^\mathrm{C})\left\{\frac{G_\mathrm{S}}{G_\mathrm{T}}\right\}^\eta, \tag{12a}$$

$$G_S = G_s + G_t, \;\; G_T = G_n + G_s + G_t, \tag{12b}$$

where G_n, G_s and G_t denote parameters (fracture energies) which constitute the work done by the tractions and their conjugate relative displacement (in the normal, first and second shear directions); G^C denotes (mixed-mode) critical fracture energy; G_n^C, G_s^C and G_t^C are the parameters of critical fracture energies causing failure (in the normal, first and second shear directions); G_S represents the amount of total work done by the shear traction and the corresponding relative displacement components; G_T is the total work done by the normal and shear traction based on energies; and η represents the cohesive property parameter.

For the linear approach under damage evolution, in the framework of numerical simulations, the damage parameter is presented as [46, 73]:

$$D = \frac{\delta_m^f(\delta_m^{max} - \delta_m^0)}{\delta_m^{max}(\delta_m^f - \delta_m^0)} \tag{13}$$

where $\delta_\mathrm{m}^\mathrm{f}$, δ_m^0 and $\delta_\mathrm{m}^\mathrm{max}$ represent the parameters of effective separation at complete failure ($\delta_\mathrm{m}^\mathrm{f} = 2G^\mathrm{C}/T^0_\mathrm{eff}$, and T^0_eff denotes the effective traction at damage initiation), at damage initiation, as well as at the maximum measured value during loading history.

In order to better represent the CZM, Fig. 5 shows the constitutive traction-separation law – CZM [46].

DOI 10.2478/ama-2023-0015

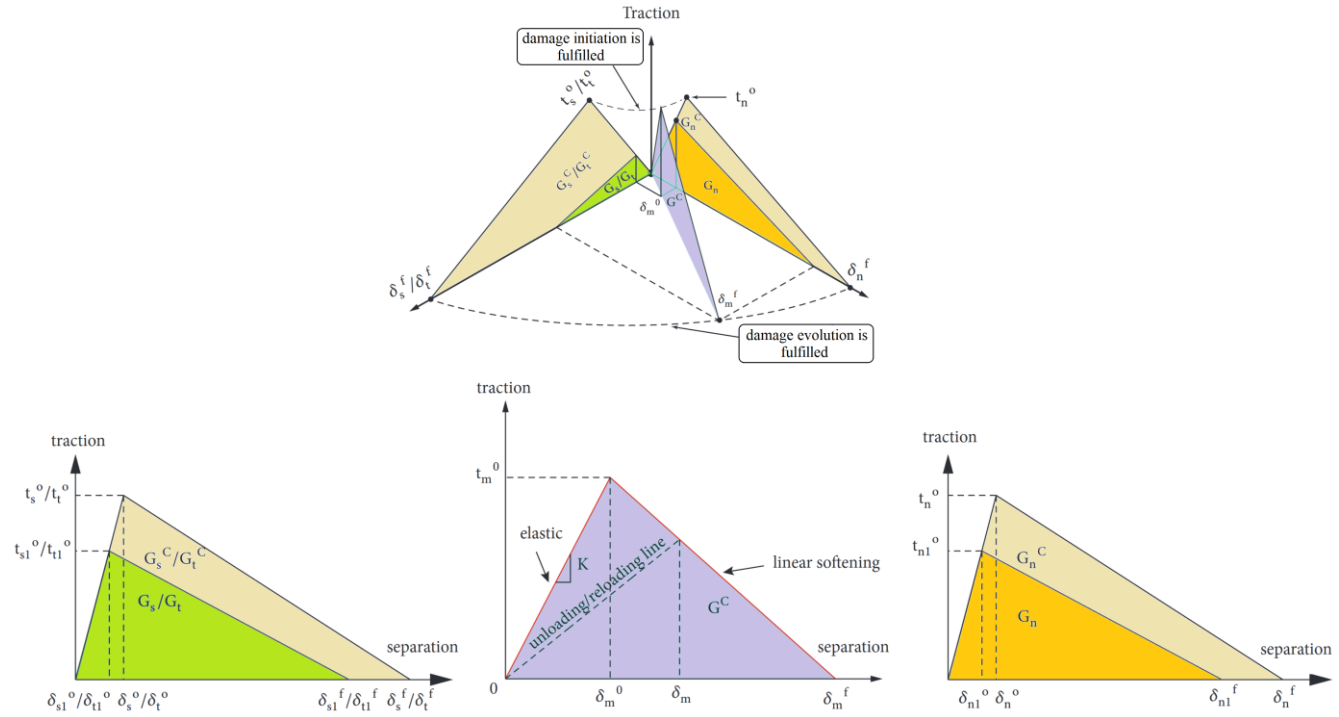

Fig. 5. Constitutive traction-separation law – CZM

The second damage model that was used in the study was the XFEM model. The MAXS criterion was used to determine the beginning of crack initiation phenomenon. Modelling discontinuities (crack) with the conventional FEM demands that the mesh conforms to the geometric discontinuities. Consequently, the XFEM was introduced (alleviates the need to create a conforming mesh). The present method was initially introduced in the framework of paper [74], which was a further extension of the method based on the concept of partition of unity [75] that allows local enrichment functions to be easily incorporated using FE approximation. The presence of (eventually) discontinuities is ensured using the enriched functions in conjunction (with additional degrees of freedom). The above-mentioned model is very attractive to simulate initiation as well as propagation of a discrete crack process. The XFEM method alleviates some deficiencies closely associated with meshing crack surfaces [74]. The damage simulation method described above enables simulating the propagation of discontinuities independently of the original FE mesh. The propagation of discontinuities (cracking) is represented by a displacement approximation function which was expressed as follows [73, 76, 77]:

$$u = \sum_{i=1}^{N} N_i(x)[u_i + H(x)a_i + \sum_{\alpha=1}^{4} F_\alpha(x) b_i^\alpha] \tag{14}$$

where $N_i(x)$ constitutes the usual nodal (displacement) shape functions; u_i represents the usual nodal displacement vector which was closely associated with the continuous part of the FE solution; a_i is additional degree of freedom of the element node penetrated by the crack tip; $H(x)$ denotes the discontinuous jump function – across the crack surfaces; b_i^α is vector of enriched nodes degree of freedom; and $F_\alpha(x)$ denotes the elastic asymptotic crack-tip functions (approximate expression of displacement field function at the crack tip).

The discontinuous jump function $H(x)$ is given the form [76, 77]:

$$H(x) = \begin{cases} +1, & if\ (x - x^*) \cdot n \geq 0 \\ -1, & otherwise \end{cases} \tag{15}$$

where x defines a Gaussian integration point; x^* denotes the point on the crack closest to x; n is the normal vector outside the crack at x^*; and $H(x)$ indicates the element penetrated by the crack surface (which is 1 on the positive, and −1 on the negative side of the crack).

In addition, the crack tip local coordinate system [73, 76] is presented in Fig. 6 for better understanding of the issues described.

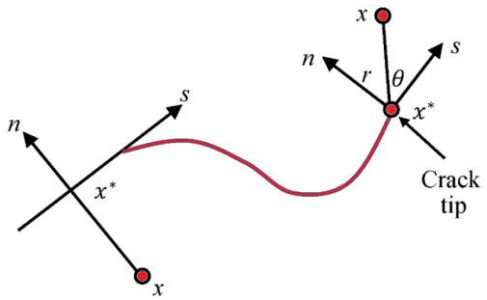

Fig. 6. Crack tip local coordinate system

The asymptotic crack tip functions in elastic material (approximate expression of displacement field function at the crack tip) $F_\alpha(x)$, is presented as [76, 77]:

$$F_\alpha(x) = \left[\sqrt{r} \cdot sin\frac{\theta}{2}, \sqrt{r} \cdot cos\frac{\theta}{2}, \sqrt{r} \cdot sin\theta \cdot sin\frac{\theta}{2}, \sqrt{r} \cdot sin\theta \cdot cos\frac{\theta}{2}\right] \tag{16}$$

where (r, θ) denote a local polar coordinate system defined and the crack tip (with its origin at the crack tip) θ=0 is tangent to the

crack at the tip.

In the case of simulation of crack growth (using the XFEM technique), it is necessary to define both damage initiation (fracture initiation) as well as damage evolution criterion of the materials. Crack initiation (damage initiation) refers to the beginning of degradation of the cohesive response directly at an enriched element. Moreover, the degradation process begins when the stresses (or the strains) satisfy the specified damage initiation criteria. In the case of this study, the MAXS criterion was used (corresponding to the damage initiation criterion for the CZM, as described earlier). The above-mentioned criterion can be represented as [73, 77]:

$$f = max\left\{\frac{\langle t_n \rangle}{t_n^0}, \frac{t_s}{t_s^0}, \frac{t_t}{t_t^0}\right\}. \quad (17)$$

where t_n, t_s, t_t are the normal and two shear component to the likely cracked surface; t_n^0, t_s^0, t_t^0 – are the peak values of the nominal stress; ⟨ ⟩ denotes Macaulay bracket (used to signify that a purely compressive stress state does not cause (initiate) damage; and damage is assumed to initiate when the MAXS ratio reaches a value of 1).

Similarly to the previous description concerning the CZM, when the damage initiation is satisfied, further loading of the composite structure causes damage evolution phenomenon (based on the energy criterion). When damage initiation criterion is achieved, a linear energy-based softening controlled by the B–K-Law is applied [41, 77], as was in the case with the previously described CZM damage model. Numerical simulations (using FEM) were carried out based on the prepared numerical model which considered previously described damage simulation techniques (CZM and XFEM). In the numerical simulations, the aforementioned two damage models were applied simultaneously within the numerical model in order to allow for both delamination (CZM) and material fracture (XFEM) damage phenomena of the composite material. In this study, the material model of Lamina type (elastic parameters with fail stress) was used. The composite material had orthotropic properties (where basic material data are shown in Tab. 1). Regarding the use of two advanced damage models, the parameters of the CZM as well as XFEM [78] were applied, as presented in Tab. 2.

Tab. 2. CZM and XFEM parameters

Damage initiation stress in normal direction t_n [N/mm^2]	Damage initiation stress in normal direction t_s, t_t [N/mm^2]	Fracture energy in normal direction G_n^C [N/mm]	Fracture energy in first and second shear direction G_s^C, G_t^C [N/mm]
18	14	0.32	0.68

During the preparation of the numerical model, each of the eight composite layers (the thickness of each layer was 0.131 mm) was modelled separately. The composite structures are usually modelled using the method of modelling the laminate as a multilayer composite, modelled using the Conventional or Continuum Shell method [19, 67]. The above approach in modelling of the composite structure allowed the simulation of complex failure phenomena, including delamination and material cracking. The composite structure was prepared using *3D Stress* technique – based on regular hexagonal mesh, using solid FEs *C3D8R* (where each of the FE is characterised by having 8-nodes, 3 degrees of freedom in each node of the FE, linear shape function and reduced integration). In addition, three identical non-deformable objects used to support the deformable composite structure were modelled in the numerical simulations. The non-deformable cylindrical objects were modelled using *R3D4* FEs (each of the FE is characterised by having four nodes and three translational degrees of freedom in each node of the FE). The discrete model consisted of a total of 19,272 FEs (16,200 linear hexahedral elements of type C3D8R and 3,072 linear quadrilateral elements of type R3D4) and 37,984 computational nodes. The cohesive surfaces (considering cohesive behaviour with stiffness parameters), normal and tangential behaviour (without friction), as well as damage with damage initiation and evolution parameters) were implemented between all laminate layers (a total of seven cohesive surfaces). In addition, each layer was assigned the possibility of a cracking phenomenon, depending on the material strength according to the XFEM model which allows the simulation of the fracture phenomenon. Moreover, the contact interactions (in normal and tangential direction) between the non-deformable objects and the composite structure, with the friction 0.1 were also defined. The boundary conditions were applied at specially generated reference points, which were coupled to non-deformable cylindrical objects. The top non-deformable object was assigned boundary conditions under which it was allowed to move only in the direction of the composite specimen relative to the Z-axis. The bottom non-deformable objects had all degrees of freedom locked. This approach made it possible to simulate the three-point bending phenomenon of the composite specimen. The boundary conditions and discrete model are presented in Fig. 7.

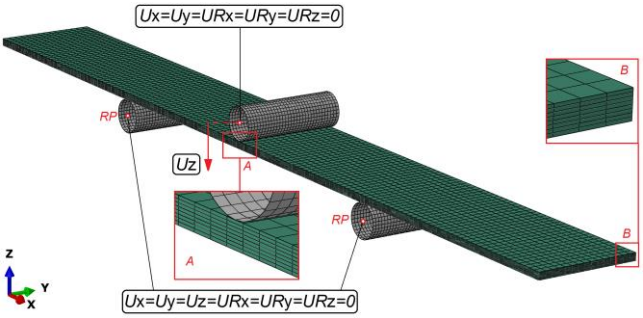

Fig. 7. Discrete model of composite profile with boundary conditions

3. RESULTS

In this section, both the results of the three-point bending as well as damage initiation and evolution of the failure mechanism will be presented in detail. The results of failure will be presented on the basis of experimental investigations using UTM and digital microscope as well as non-linear numerical simulations using two independent damage models (CZM and XFEM). In the case of experimental tests, curves describing the course of the load versus displacement, registered directly with the load cell – Fig. 8.

In the course of the conducted three-point bending tests, during the movement (displacement in the direction of the composite specimen) of the test head, the force acting on the composite structure was registered. Consequently, experimental curves (load–displacement) were determined for all six actual specimens.

Fig. 8. Test stand prepared for three-point bending tests

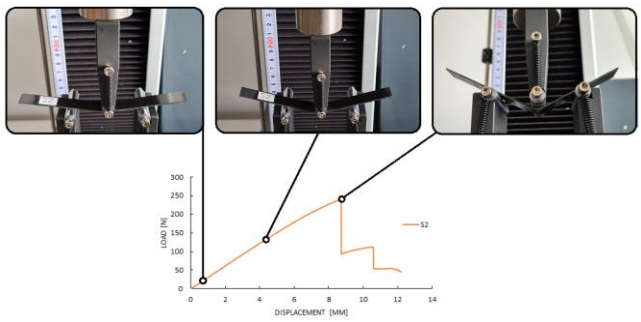

Fig. 9. Determination of load–displacement curves

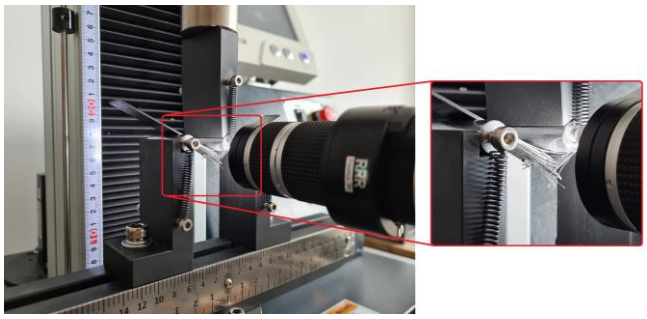

Fig. 10. Recording of composite material failure form

Fig. 9 shows the stages of loading the structure until it collapses. The structure worked elastically until a rapid loss of load-carrying capacity (displacement slightly exceeding 8.5 mm), followed by a complex phase of failure. Experimental investigations allowed both the determination of load–displacement curves for each test specimen and the evaluation of the form of structural failure of the composite material using a mobile head of the digital microscope. The above-mentioned mobile microscope head made it possible to record complex forms of failure, for all test specimens, using a 30× zoom (Fig. 10.).

The recorded forms of failure were then stored in the memory of the computer controlling the digital microscope. This approach allowed comparison of the obtained forms of failure of the composite material structure for all test specimens, with further possibility of comparison with the result of numerical simulation. In the case of the numerical simulations, the actual boundary conditions were fully reproduced, and the additional consideration of the previously described independent failure models enabled a comprehensive evaluation of the failure phenomenon during the three-point bending test. Within the framework of numerical simulations, the curve describing the course of the load versus displacement was determined, which allowed comparison with the experimental results.

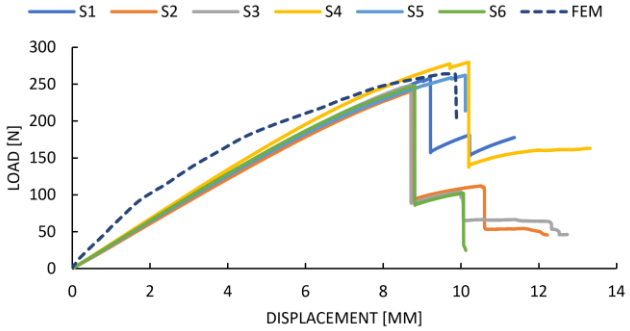

Fig. 11. Comparison of experimental load–displacement curves with FEM simulation result

On the basis of the conducted tests, very good agreement was observed in the qualitative aspect of the results, both between the individual experimental tests and the numerical simulation result. The highest value of load corresponding to loss of load-carrying capacity was observed for the specimen designated S4, for which the failure force was about 279.79 N. The lowest failure force was 240.75 N and related to specimen S2. The maximum discrepancy between the failure load results in the context of the experimental study was about 14%. The experimental specimen, designated as S4, shows a significantly higher ultimate load value than the other five specimens, which significantly affects the maximum discrepancy of the results of the loads corresponding to the loss of load-carrying capacity. If only the values of all the experimental specimens except S4 were compared, the maximum discrepancy would decrease significantly. Regarding the numerical simulation, it was observed that the maximum value of the failure force was 264.05 N. The discrepancy between the average value of failure force of the experimental study and the FEM simulation result was 3%. The above indicates a very precise preparation of the numerical model in terms of quantitative evaluation of research results. Tab. 3 shows the values of the failure loads.

The measurable effect of experimental studies and numerical simulations was the qualitative evaluation of the obtained forms of failure. For the experimental tests, complex failure forms were registered for each test specimen, which was finally compared with the FEA results. The forms of failure observed during the experimental tests conducted are shown in Fig. 12.

DOI 10.2478/ama-2023-0015

Tab. 3. Limit load values

Experimental study [N]	Average value of experimental study [N]	Numerical study [N]
S1 – 258.39	256.33	264.05
S2 – 240.75		
S3 – 248.93		
S4 – 279.79		
S5 – 262.17		
S6 – 247.92		

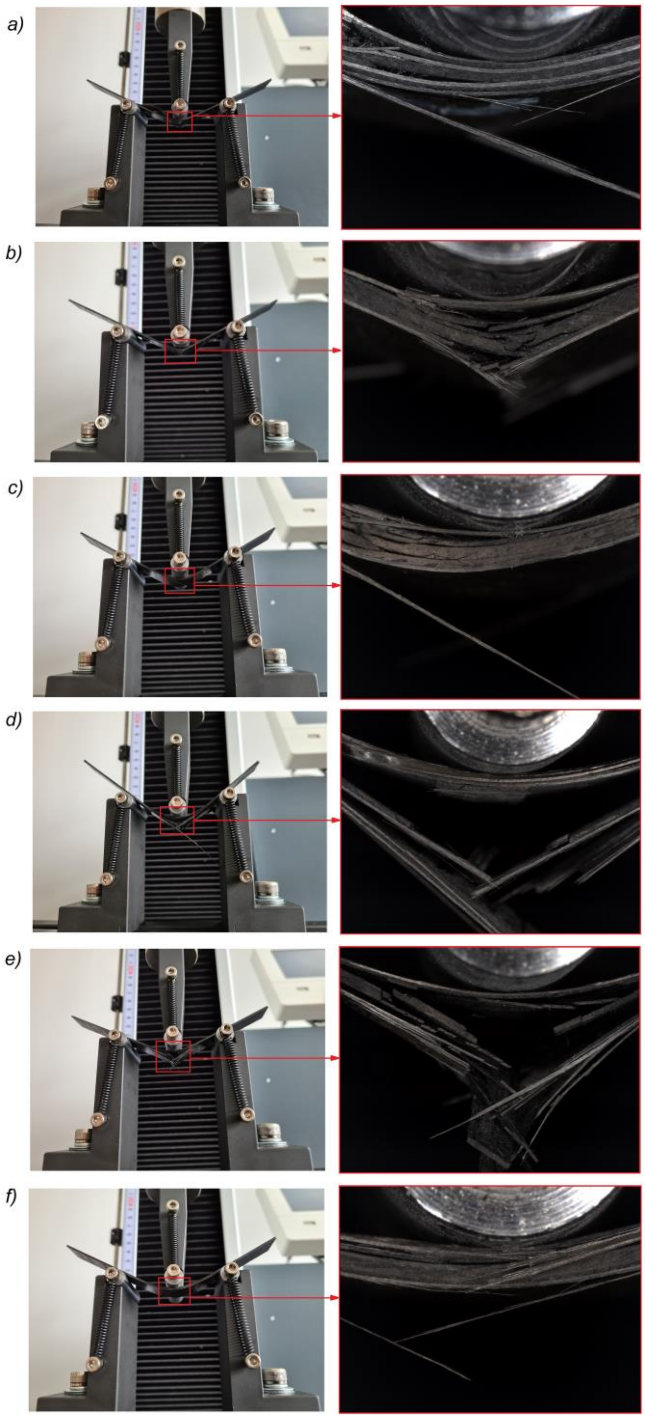

Fig. 12. Experimentally determined failure forms for individual specimens: (a) S1, (b) S2, (c) S3, (d) S4, (e) S5 and (f) S6

In each of the analysed cases, a complex failure mechanism of the composite material was observed. It was observed that delamination, fibre cracking (due to fibre bending) and matrix crushing occurred. Although all of the experimental specimens had the same composite lay-up, the failure forms (or rather, the propagation of these forms) were slightly different. However, this had no significant effect on the discrepancy of the limit loads presented previously. The dominant failure form occurred in the central part of the test specimen, in the area at which the load from the testing machine head was generated. The use of a mobile head of digital microscope allowed for precise recording of the failure forms. Simultaneously conducted numerical simulations made it possible to compare the test results in the context of qualitative assessment. Fig. 13 shows a complex form of structural failure of a composite material using overall scalar stiffness degradation (SDEG) parameter.

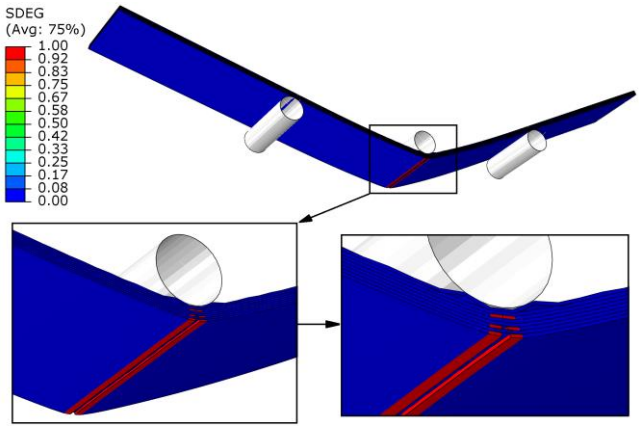

Fig. 13. Loss of load-carrying capacity of composite structure – numerical simulation result

A complex state of failure of the material structure was observed, both through the occurrence of material cracking (using the XFEM model) and delamination (using the CZM technique). Achieving a value of 1 within SDEG parameter indicates a total loss of stiffness (stiffness degradation) in a specific area. Moreover, the numerical simulation showed the damage evolution phenomenon, where initially cracking of the composite material was observed, followed by delamination phenomenon – Fig. 14.

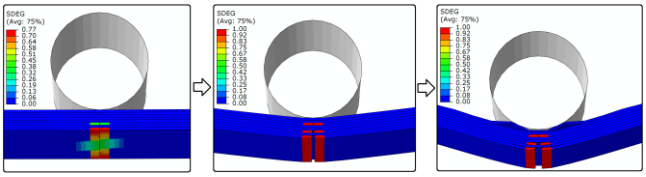

Fig. 14. Evolution of composite material failure phenomenon – simulation result

Within the framework of the conducted tests, very high agreement in terms of quality was observed between the result of the experimental tests and the numerical simulation – which is confirmed in Fig. 15.

DOI 10.2478/ama-2023-0015

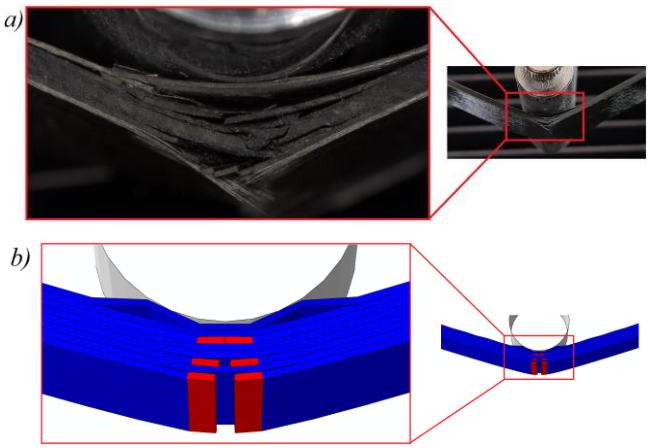

Fig. 15. Comparison of failure modes: (a) experimental tests (specimen S2) and (b) numerical simulation

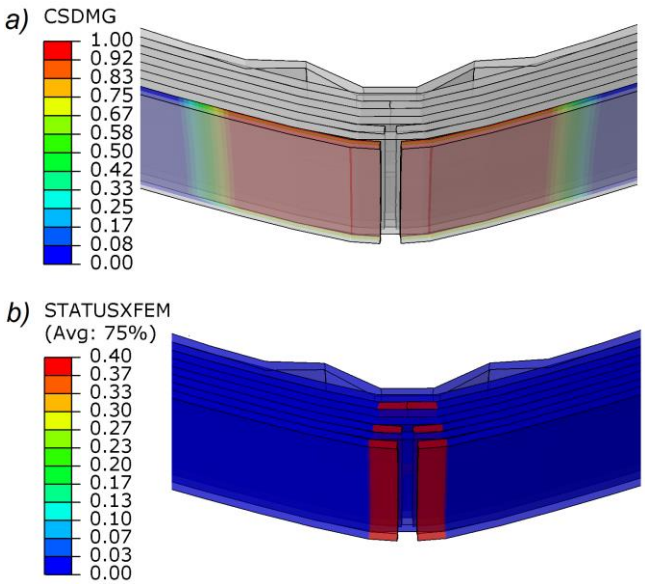

Fig. 16. Failure of composite structure: (a) CSDMG (between the two outer layers) and (b) XFEM

In the case of numerical simulations, using the two previously mentioned advanced techniques to simulate the failure phenomenon of the composite material, a complex failure mechanism adequate for the experimental studies was obtained. The results of numerical calculations provided the necessary information on the complex course of failure of the composite material. In the initial stage of damage in FEM simulations the cracking of composite material layers was observed (Fig. 14), after which, during further loading of the structure in the framework of the three-point bending test, the phenomenon of layer cracking deepened along with the occurrence of the delamination phenomenon (Fig. 15b). The layer cracking phenomenon mainly affected those layers in which the fibres of the composite material were aligned along the length of the test specimen (layers 1, 3, 6 and 8). Moreover, the results of the failure phenomenon based on the CSDMG parameter – which determines the damage evolution of the cohesive zone – and XFEM – which represents the failure due to material cracking – are presented in the numerical simulation – Fig. 16. Obviously, the delamination-induced damage occurred between all the constituent layers of the composite material; however, Fig. 16a shows an example of the result between the bottom two outer layers of the composite material.

Any permanent forms of damage that appeared, such as delamination, or the complete rupture of the layers, took place at the time of loss of load-carrying capacity – or immediately afterwards, as evidenced by the curves from the tests in Fig. 11. The numerical simulation techniques used in the study of the phenomenon of the complex mechanism of failure of the composite material, confirmed experimentally obtained forms of failure, especially in the context of qualitative assessment (quantitative agreement is shown in Fig. 11 and Tab. 3). The numerical simulation provided a virtual representation of the failure phenomenon of the composite material, including the phenomena directly contributing to the failure. Fig. 17 presents in detail the obtained form of failure during numerical simulations using FEM.

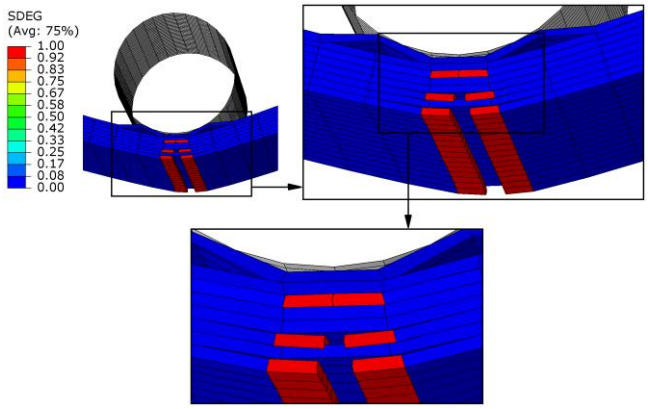

Fig. 17. Failure in terms of numerical simulation

4. CONCLUSION

The limit states of a three-point bending composite structure were determined from the tests. Based on the investigations, the following general conclusions were formulated:

- It is possible to evaluate the failure analysis, especially with regard to the delamination and crack propagation phenomena (directly preceding the loss of load-carrying capacity) of beam composite structures, using experimental investigations (UTM and digital microscope) as well as numerical simulations using FEM (especially using CZM and XFEM);
- The evaluation of limit loads (critical, damage initiation, delamination and loss of load-carrying capacity loads) allows assessment of the complex failure mechanism;
- Simultaneous use of several independent numerical damage models allows for faithful representation of the actual damage phenomenon;
- The use of a mobile digital microscope head allows recording of the complex mechanism of failure, which in turn allows comparison of failure forms with FEA.

In the context of the quantitative evaluation, it was estimated that the discrepancy of the results corresponding to the failure load between all experimental tests does not exceed 14%. This discrepancy would be even lower (<10%) if not for one of the specimens designated as S4. Moreover, the discrepancy of the average result of the failure load from the experimental tests in relation to the result from the FEM simulation was about 3%, which proves the high quality of the prepared numerical model. In

the study, a complex failure mechanism of the composite material was observed, within which both material cracking and delamination occurred – as demonstrated by the experimental studies and FEM simulations. The main failure area occurring in the central part of the composite profile (opposite to the applied load), resulting from the specific nature of the tests conducted, is an ideal example of the progressive failure of the composite material structure, in which advanced forms of damage could be observed.

Future research plans include the use of the acoustic emission method to estimate the initiation and evolution of damage to the composite material during experimental tests. This will allow, first of all, to compare the results in the context of phenomena directly affecting the loss of load-carrying capacity and to compare them with the damage initiation and evolution criteria realised within FEM.

The research presented in the paper provides the basis for the research conducted under the project No. 2021/41/B/ST8/00148 (in terms of presenting interdisciplinary research methods on composite materials), financed by the National Science Centre, Poland – on composite profiles with closed sections. The research techniques presented in this paper will be used to carry out research within the framework of the aforementioned scientific project.

REFERENCES

1. Fascetti A, Feo L, Nistic N, Penna R. Web-flange behavior of pultruded GFRP I beams: a lattice model for the interpretation of experimental results. Composites Part B Eng, 2016;100:257-269.
2. Berardi VP, Perrella M, Feo L, Cricrì G. Creep behavior of GFRP laminates and their phases: experimental investigation and analytical modeling. Composites Part B Eng, 2017;122:136-144.
3. Kubiak T, Kolakowski Z, Swiniarski J, Urbaniak M, Gliszczynski A. Local buckling and post-buckling of composite channel-section beams – numerical and experimental investigations. Composites Part B Eng, 2016;91:176-188.
4. Rozylo P. Experimental-numerical study into the stability and failure of compressed thin-walled composite profiles using progressive failure analysis and cohesive zone model. Composite Structures, 2021;257:113303.
5. Debski H, Rozylo P, Teter A. Buckling and limit states of thin-walled composite columns under eccentric load. Thin-Walled Structures, 2020;149:106627.
6. Debski H, Rozylo P, Wysmulski P. Stability and load-carrying capacity of short open-section composite columns under eccentric compression loading. Composite Structures, 2020;252:112716.
7. Rozylo P, Debski H. Stability and load-carrying capacity of short composite Z-profiles under eccentric compression. Thin-Walled Structures, 2020;157:107019.
8. Debski H, Samborski S, Rozylo P, Wysmulski P. Stability and Load-Carrying Capacity of Thin-Walled FRP Composite Z-Profiles under Eccentric Compression. Materials, 2020;13:2956.
9. Rozylo P, Debski H. Effect of eccentric loading on the stability and load-carrying capacity of thin-walled composite profiles with top-hat section. Composite Structures, 2020;245:112388.
10. Gliszczynski A, Czechowski L. Collapse of channel section composite profile subjected to bending, Part I: Numerical investigations. Compos Struct, 2017;178:383–394.
11. Jakubczak P, Gliszczynski A. Bienias J, Majerski K. Kubiak T. Collapse of channel section composite profile subjected to bending Part II: Failure analysis. Compos Struct, 2017;179:1–20.
12. Kazmierczyk F, Urbaniak M, Swiniarski J, Kubiak T. Influence of boundary conditions on the behaviour of composite channel section subjected to pure bending – Experimental study. Compos Struct, 2022;279:114727.
13. Gliszczynski A, Kubiak T. Load-carrying capacity of thin-walled composite beams subjected to pure bending. Thin-Walled Struct, 2017;115:76–85.
14. Czechowski L, Gliszczynski A, Bienias J, Jakubczak P, Majerski K. Composites Part B, 2017;111:112-123.
15. Banat D, Mania RJ. Failure assessment of thin-walled FML profiles during buckling and postbuckling response. Compos Part B Eng 2017;112:278-289.
16. Madukauwa-David ID, Drissi-Habti M. Numerical simulation of the mechanical behavior of a large smart composite platform under static loads. Composites Part B Eng 2016;88:19-25.
17. Feo L, Latour M, Penna R, Rizzano G. Pilot study on the experimental behavior of GFRP-steel slip-critical connections. Composites Part B Eng 2017;115:209-222.
18. Chroscielewski J, Miskiewicz M, Pyrzowski Ł, Sobczyk B, Wilde K. A novel sandwich footbridge - Practical application of laminated composites in bridge design and in situ measurements of static response. Composites Part B Eng 2017;126:153-161.
19. Rozylo P. Stability and failure of compressed thin-walled composite columns using experimental tests and advanced numerical damage models. Int J Numer Methods Eng. 2021;122:5076-5099.
20. Rozylo P, Wysmulski P. Failure analysis of thin-walled composite profiles subjected to axial compression using progressive failure analysis (PFA) and cohesive zone model (CZM). Composite Structures, 2021;262:113597.
21. Rozylo P, Debski H, Wysmulski P, Falkowicz K. Numerical and experimental failure analysis of thin-walled composite columns with a top-hat cross section under axial compression. Composite Structures 2018;204:207-216.
22. Paszkiewicz M, Kubiak T. Selected problems concerning determination of the buckling load of channel section beams and columns. Thin-Walled Structures 2015;93:112-121.
23. Ascione F. Influence of initial geometric imperfections in the lateral buckling problem of thin walled pultruded GFRP I-profiles. Composite Structures 2014;112:85–99.
24. Sohn MS, Hu XZ, Kim JK, Walker L. Impact damage characterisation of carbon fibre/epoxy composites with multi-layer reinforcement. Composites Part B: Engineering 2000;31:681-691.
25. Batra RC, Gopinath G, Zheng JQ. Damage and failure in low energy impact of fiber-reinforced polymeric composite laminates. Composite Structures 2012;94:540-547.
26. Rozylo P, Ferdynus M, Debski H, Samborski S. Progressive Failure Analysis of Thin-Walled Composite Structures Verified Experimentally. Materials, 2020;13:1138.
27. Debski H, Rozylo P, Gliszczynski A, Kubiak T. Numerical models for buckling, postbuckling and failure analysis of predamaged thin-walled composite struts subjected to uniform compression. Thin-Walled Structures, 2019;139:53-65.
28. Reddy JN, Pandey AK. A first-ply failure analysis of composite laminates. Comput Struct, 1987;25:371–393.
29. Kubiak T, Samborski S, Teter A. Experimental investigation of failure process in compressed channel-section GFRP laminate columns assisted with the acoustic emission method. Compos Struct, 2015; 133:921-929.
30. Hashin Z, Rotem A. A fatigue failure criterion for fibre reinforced materials. J. Compos. Mater, 1973;7:448–464.
31. Camanho PP, Maimí P, Dávila CG. Prediction of size effects in notched laminates using continuum damage mechanics. Compos. Sci. Technol, 2017;67:2715–2727.
32. Camanho PP, Matthews FL. A progressive damage model for mechanically fastened joints in composite laminates. J. Comp. Mater, 1999;33:2248–2280.

33. Barbero EJ, Cosso FA. Determination of material parameters for discrete damage mechanics analysis of carbon epoxy laminates. Compos. Part B Eng, 2014;56:638–646.
34. Lemaitre J, Plumtree A. Application of damage concepts to predict creep fatigue failures. J. Eng. Mater. Technol, 1979;101:284–292.
35. Ribeiro ML, Vandepitte D, Tita V. Damage model and progressive failure analyses for filament wound composite laminates. Appl. Compos. Mater, 2013;20:975–992.
36. Kachanov LM. Time of the rupture process under creep conditions, Izv. AN SSSR. Otd. Tekh. Nauk, 1958;8:26–31.
37. Matzenmiller A, Lubliner J, Taylor LR. A constitutive model for anisotropic damage in fiber composites. Mech. Mater, 1995;20:125–152.
38. Lapczyk I, Hurtado JA. Progressive damage modeling in fiber-reinforced materials. Compos. Part A Appl. Sci. Manuf, 2007;38: 2333–2341.
39. Bisagni C, Di Pietro, G, Fraschini L, Terletti D. Progressive crushing of fiber reinforced composite structural components of a Formula One racing car. Compos. Struct, 2005;68:491–503.
40. Li W, Cai H, Li C, Wang K, Fang L. Progressive failure of laminated composites with a hole under compressive loading based on micro-mechanics. Adv. Compos. Mater, 2014;23:477–490.
41. Benzeggagh ML, Kenane M. Measurement of Mixed-Mode Delamination Fracture Toughness of Unidirectional Glass/Epoxy Composites with Mixed-Mode Bending Apparatus. Composites Science and Technology, 1996;56:439–449.
42. Dugdale DS. Yielding of steel sheets containing slit, Journal of the Mechanics and Physics of Solids, 1960;8(2):100-104.
43. Barenblatt GI. The mathematical theory of equilibrium cracks in brittle fracture. Advances in Applied Mechanics, 1962;7:55-129.
44. Turon A, Camanho PP, Costa J, Dávila CG. A damage model for the simulation of delamination in advanced composites under variable-mode loading, Mechanics of Materials, 2006;38(11):1072-1089.
45. Camanho PP, Davila CG, de Moura MF. Numerical simulation of mixed-mode progressive delamination in the composite materials, Journal of Composite Materials, 2003;37(16):1415-1438.
46. Hu H, Niu F, Dou T, Zhang H. Rehabilitation Effect Evaluation of CFRP-Lined Prestressed Concrete Cylinder Pipe under Combined Loads Using Numerical Simulation. Mathematical Problems in Engineering, 2018;2018:3268962.
47. Borg R, Nilsson L, Simonsson K. Simulating DCB, ENF and MMB experiments using shell elements and a cohesive zone model, Composites Science and Technology, 2004;64:269-278.
48. Zhao L, Gong Y, Zhang J, Chen Y, Fei B. Simulation of delamination growth in multidirectional laminates under mode I and mixed mode I/II loadings using cohesive elements, Composite Structures, 2014; 116:509-522.
49. Rozylo P. Failure analysis of thin-walled composite structures using independent advanced damage models. Composite Structures, 2021;262:113598.
50. Li ZM, Qiao P. Buckling and postbuckling behavior of shear deformable anisotropic laminated beams with initial geometric imperfections subjected to axial compression. Engineering Structures, 2015;85:277–292.
51. Bouhala L, Makradi A, Belouettar S, Younes A, Natarajan S. An XFEM/CZM based inverse method for identification of composite failure parameters. Comput. Struct, 2015;153:91-97.
52. Paneretti E, Fanteria D, Danzi F. Delaminations growth in compression after impact test simulations: Influence of cohesive elements parameters on numerical results. Compos. Struct, 2016;137:140-147.
53. Moes N, Dolbow J, Belytschko T. A finite element method for crack growth without remeshing. Int J Numer Methods Eng, 1999;46(1):131–50.
54. Moës N, Belytschko T. Extended finite element method for cohesive crack growth. Eng Fracture Mech, 2002;69(7):813–33.
55. Dolbow J, Moës N, Belytschko T. An extended finite element method for modeling crack growth with frictional contact. Comput Methods Appl Mech Eng, 2001;190(51-52):6825–46.
56. Melenk J, Babuska I. The partition of unity ˙nite element method: Basic theory and applications. computer methods. Appl. Mech Eng, 1996;39:289–314.
57. Zienkiewicz OC, Taylor RL. Finite Element Method—Solid Mechanics, 5th ed.; Elsevier: Barcelona, Spain, 2000.
58. Parlapalli MR, Soh KC, Shu DW, Ma G. Experimental investigation of delamination buckling of stitched composite laminates. Composites: Part A, 2007;38:2024–2033.
59. Turvey GJ, Zhang Y. A computational and experimental analysis of the buckling, postbuckling and initial failure of pultruded GRP columns. Composite Structures, 2006;84:1527–1537.
60. Bohse J. et al. Damage analysis of Polymer Matrix Composites by Acoustic Emission Testing. DGZfP-Proceedings BB 90-CD:339-348.
61. Riccio A, Saputo S, Sellitto A, Di Caprio F, Di Palma L. A numerical-experimental assessment on a composite fuselage barrel vertical drop test: Induced damage onset and evolution. Composite Structures, 2020;248:112519.
62. Gliszczynski A, Kubiak T. Progressive failure analysis of thin-walled composite columns subjected to uniaxial compression. Composite Structures, 2017;169:52-61.
63. Aveiga D, Ribeiro ML. A Delamination Propagation Model for Fiber Reinforced Laminated Composite Materials. Mathematical Problems in Engineering, 2018;2018:1861268.
64. Rozylo P, Debski H, Falkowicz K, Wysmulski P, Pasnik J, Kral J. Experimental-Numerical Failure Analysis of Thin-Walled Composite Columns Using Advanced Damage Models. Materials, 2021;14(6): 1506.
65. Banat D, Mania RJ, Degenhardt R. Stress state failure analysis of thin-walled GLARE composite members subjected to axial loading in the post-buckling range. Composite Structures, 2022;289:115468.
66. Banat D, Mania RJ. Damage analysis of thin-walled GLARE members under axial compression – Numerical and experiment investigations. Compos. Struct, 2020;241:112102.
67. Debski H. Experimental investigation of post-buckling behavior of composite column with top-hat cross-section. Eksploat. Niezawodn, 2013;15:106–110.
68. Debski H. Badania numeryczne i doświadczalne stateczności i nośności kompozytowych słupów cienkościennych poddanych ściskaniu. Zeszyty naukowe nr 1161, Wydawnictwo Politechniki Łódzkiej, ISSN 0137-4834, Łódź, 2013.
69. Rozylo P. Comparison of Failure for Thin-Walled Composite Columns. Materials, 2022;15:167.
70. Debski H, Rozylo P, Wysmulski P, Falkowicz K, Ferdynus M. Experimental study on the effect of eccentric compressive load on the stability and load-carrying capacity of thin-walled composite profiles. Composites Part B, 2021;226:109346.
71. Li Z, Cen S, Wu CJ, Shang Y, Li CF. High-performance geometric nonlinear analysis with the unsymmetric 4-node, 8-DOF plane element US-ATFQ4. Int J Numer Methods Eng, 2018;114:931–954.
72. Camanho PP, Davila CG. Mixed-mode decohesion finite elements for the simulation of delamination in composite materials. NASA/TM-2002–211737, 2002:1–37.
73. Dassault Systemes Simulia Corp. Abaqus 2020 Documentation. Providence, RI, USA, 2020.
74. Belytschko T, Black T. Elastic Crack Growth in Finite Elements with Minimal Remeshing. International Journal for Numerical Methods in Engineering, 1999;45:601–620.
75. Melenk J, Babuska I. The Partition of Unity Finite Element Method: Basic Theory and Applications. Computer Methods in Applied Mechanics and Engineering, 1996;39:289–314.
76. Yu Z, Zhang J, Shen J, Chen H. Simulation of crack propagation behavior of nuclear graphite by using XFEM, VCCT and CZM methods. Nuclear Materials and Energy, 2021;29:101063.

77. Heidari-Rarani M, Sayedain M. Finite element modeling strategies for 2D and 3D delamination propagation in composite DCB specimens using VCCT, CZM and XFEM approaches. Composites Part C: Open Access, 2020;2:100014.
78. Kolanu NR, Raju G, Ramji M. A unified numerical approach for the simulation of intra and inter laminar damage evolution in stiffened CFRP panels under compression. Composites Part B, 2020;190: 107931.

Acknowledgments: The research was conducted under project No. 2021/41/B/ST8/00148, financed by the National Science Centre, Poland.

Patryk Różyło: https://orcid.org/0000-0003-1997-3235